Drift characteristics and the multi-field coupling stress mechanism of the pantograph-catenary arc under low air pressure

Zhilei Xu(许之磊)[1], Guoqiang Gao(高国强)[1,†], Pengyu Qian(钱鹏宇)[1], Song Xiao(肖嵩)[1], Wenfu Wei(魏文赋)[1], Zefeng Yang(杨泽锋)[1,2], Keliang Dong(董克亮)[1], Yaguang Ma(马亚光)[1], and Guangning Wu(吴广宁)[1]

[1] *School of Electrical Engineering, Southwest Jiaotong University, Chengdu* 610031, *China*
[2] *Research and Development Department, Chengdu Guojia Electrical Engineering Co. Ltd, Chengdu* 611756, *China*

(Received 6 July 2022; revised manuscript received 7 September 2022; accepted manuscript online 21 September 2022)

The fault caused by a pantograph-catenary arc is the main factor that threatens the stability of high-speed railway energy transmission. Pantograph-catenary arc vertical drift is more severe than the case under normal pressure, as it is easy to develop the rigid busbar, which may lead to the flashover occurring around the support insulators. We establish a pantograph-catenary arc experiment and diagnosis platform to simulate low pressure and strong airflow environment. Meanwhile, the variation law of arc drift height with time under different air pressures and airflow velocities is analyzed. Moreover, arc drift characteristics and influencing factors are explored. The physical process of the arc column drifting to the rigid busbar with the jumping mechanism of the arc root on the rigid busbar is summarized. In order to further explore the mechanism of the above physical process, a multi-field stress coupling model is built, as the multi-stress variation law of arc is quantitatively evaluated. The dynamic action mechanism of multi-field stress on arc drifting characteristics is explored, as the physical mechanism of arc drifting under low pressure is theoretically explained. The research results provide theoretical support for arc suppression in high-altitude areas.

Keywords: pantograph-catenary arc, low pressure, multi-field stress coupling model, arc column drift

PACS: 52.80.Mg, 52.77.Fv **DOI:** 10.1088/1674-1056/ac9360

1. Introduction

As a sliding electrical contact material, carbon–copper electrodes have high current transmission efficiency, low contact resistance, and excellent crocking resistance, as they are widely implemented in many fields, such as rail transportation and aerospace.[1–5] A carbon–copper electrode is the core element of a pantograph-catenary sliding electrical contact system in the field of rail transit, and it is also subjected to vibration impact, which leads to the arcing phenomenon occurring frequently. According to statistics, the fault caused by pantograph-catenary arcs is the main factor that threatens the power supply's safety, and the loss is very serious.[6–9] High-speed trains would suffer from various environments or conditions, such as the Sichuan–Tibet railway, which will operate under low pressure and strong airflow for a long time, the frequency of arc occurrence is higher, the arcing time is longer, and the vertical arc drift is more serious. The arc column vertical drift causes the arc to develop on the rigid busbar, which leads to the busbar ablation and mechanical performance degradation. In addition, due to small insulation spacing of a rigid pantograph-catenary system, the arc is easy to float to the vicinity of the supporting insulator, which will cause flashover to occur around the support insulators.[10,11] However, the characteristics and influencing factors of the vertical drift of the arc column in the low air pressure and strong airflow environment are still unclear. The physical process of the arc column drift to the rigid busbar and the multi-stress variation law of the pantograph-catenary arc in the movement process are rarely reported. Therefore, it is of great significance to study drift characteristics of pantograph-catenary arc and the mechanism of multi-field coupling stress for suppressing arc drift and realizing arc control in low air pressure and strong airflow.

At present, scholars at home and abroad have carried out a lot of research on the arc motion characteristics and its influence mechanism under different air pressures, mainly focusing on switching electrical arc,[12–16] UHV secondary arc[17,18] and pantograph-catenary arc,[10,19–27] and so on,[28] many achievements have been made. Research on arc characteristics under low air pressure mainly focuses on vacuum circuit breaker arc and the arc under extremely low air pressure (< 0.3 atm) environment.[14,16,29] However, it is still unclear what differences the arc motion characteristics will show at air pressures between 0.5 atm and 0.8 atm. In Refs. [17,18], the authors studied the effect of different airflow velocities on the motion characteristics of UHV secondary arc, considering that the airflow velocity is about 5 m/s, whereas the airflow velocity at the carbon slide of the pantograph-catenary system can reach about 30 m/s. The influence mechanism of airflow on arc drift is very different. In terms of chain arc modeling, the authors of Ref. [30] explored the multi-field stress characteristics of the high-altitude DC insulator's local arc. However, the arc current of the pantograph-catenary is about 10^7 times that

†Corresponding author. E-mail: xnjdggq@163.com
© 2023 Chinese Physical Society and IOP Publishing Ltd

of the local arc current of the insulator, and the multi-stress action mechanism of the arc is very different from that of the pantograph-catenary arc. It can be seen from the review that there is no relevant research on the vertical drift characteristics of the pantograph-catenary arc and its influencing mechanism and the multi-stress mechanism in the low air pressure and strong airflow environment.

To this end, the experimental platform of pantograph-catenary arc under low air pressure and strong airflow is built in this paper, the development process and vertical drift characteristics of pantograph-catenary arc under different air pressure and different airflow velocity are analyzed, and the physical process of the arc column drift to the busbar and the jumping mechanism of the arc root on the busbar are summarized. Based on the comprehensive consideration of the electromagnetic force, thermal buoyancy, wind load, and air resistance of the pantograph-catenary arc under low air pressure and strong airflow, a numerical calculation model of the multi-field coupling stress of the pantograph arc is established. The multi-stress variation law of arc under different air pressure and airflow is analyzed, the multi-field coupling stress of pantograph-catenary arc in different development stages is theoretically calculated, and the action mechanism of multi-field coupling stress on arc drifting movement in different development stages is revealed. The research results provide theoretical support for arc suppression in high-altitude areas.

2. Drift characteristics of pantograph-catenary arc in low air pressure and strong airflow

2.1. Experimental platform and methods

An experimental platform for pantograph-catenary arc simulating in the low air pressure and strong airflow environment was established, and the schematic diagram of the experimental platform is shown in Fig. 1.

The experimental platform consists of a constant current power supply, current limiting resistor, arc generator, oscilloscope, high-speed camera, and computer terminal. The low air pressure arc generator mainly includes a low air pressure chamber, carbon–copper electrodes, a precision displacement table, and a displacement controller, where the precision displacement table is controlled by a stepper motor controller.

The carbon–copper electrodes were pretreated before the experiment to ensure the accuracy of the experimental results. During the experiment, the carbon–copper electrode was fixed on the precision displacement table and was contacted with a gap distance of 0 mm. Then operate the precision displacement table to separate the carbon–copper electrode to generate the pantograph-catenary arc. The breaking speed of the precision displacement table is adjustable from 0 to 10 cm/s. The experiment uses a step-less speed control fan, and the airflow velocity is continuously adjustable in the range of 0–60 m/s. The position of the fan outlet is fixed at 10 cm from the electrode, and the central axis of the fan outlet is parallel to the contact point of the carbon–copper electrode to ensure that the high-speed airflow is parallel to the electrode streamline. In the experiment, the airflow velocity was controlled by adjusting the fan switch, the airflow velocity at the electrode was measured with a precision anemometer, the average value was repeated 5 times to eliminate the error, and the airflow velocity at the electrode was determined to be 10 m/s, 20 m/s, and 30 mm/s. The maximum output current of the power supply is 150 A, which is consistent with the traction current of a single pantograph when the high-speed train is running. The experiment uses a digital oscilloscope (Tektronix MDO3024, the bandwidth frequency is 200 MHz) to record the voltage waveform. Arc current was recorded using a Hall current sensor (WHK LB5S2) and an active voltage probe (Tektronix TAP0250). A high-speed camera (FASTCAM Nova S6) was used to capture the arc motion development process.

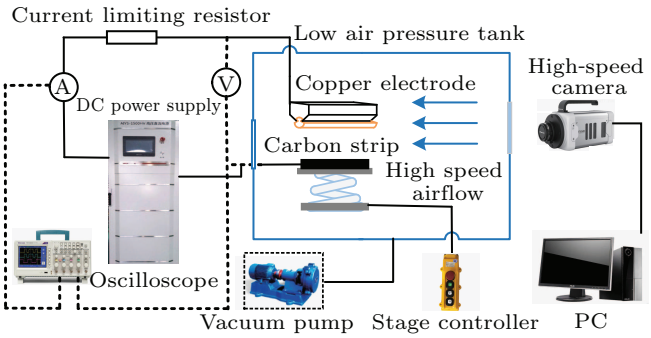


Fig. 1. Pantograph-catenary arc test and diagnosis platform under low air pressure.

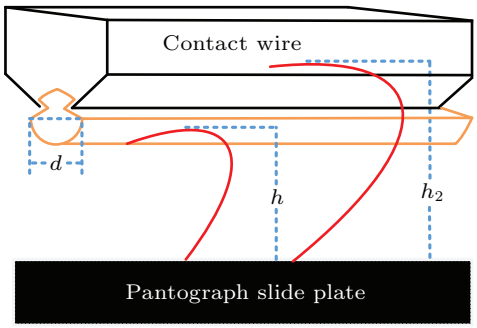


Fig. 2. Vertical arc drift height diagram.

The vertical drift height-time characteristic curve and the vertical drift velocity are important parameters to explore the drift characteristics of the arc column. The measurement schematic diagram and calculation method are shown in Fig. 2. The height of the arc column is measured using the arc image captured by the high-speed camera. Define h as the arc vertical drift height at time t_1, select the contact line diameter d_1 on the unified focal plane as the reference, d is the contact line diameter on the arc image at time t_1, then the arc vertical drift

height h_1 at time t_1 reads

$$h_1 = \frac{d_1 h}{d}. \tag{1}$$

Similarly, the arc vertical drift height h_2 at time t_2 can be calculated from the arc image, and the arc column vertical drift velocity reads

$$v = \frac{h_2 - h_1}{t_2 - t_1}. \tag{2}$$

2.2. Development process to the rigid busbar of pantograph-catenary arc

We utilize a high-speed camera to capture the development process of the pantograph-catenary arc in the low air pressure and strong airflow (P = 60 kPa; V = 30 m/s), as shown in Fig. 3. At the initial stage of arcing (t < 400 ms), the cathodic arc root and anode arc root of the pantograph-catenary arc move near the midline of the arc starting position, macroscopically showing an approximate circular "bright spot". With the development of the pantograph-catenary arc, the arc column is stretched laterally under the action of airflow. Statistics show that when the arcing time is about t = 500 ms, the transverse stretching distance of the arc column is 15.3 mm. At this time, the vertical arc drifting development of the arc is still relatively slow, and the drifting height of the arc column is about 8.3 mm. When the arc develops to about 750 ms, the heights of the arc lateral development and vertical drift arc further increase to 20.6 mm and 15 mm, and it can be observed that the arc column vertically drifts to the rigid busbar, and a new anode arc root is formed.

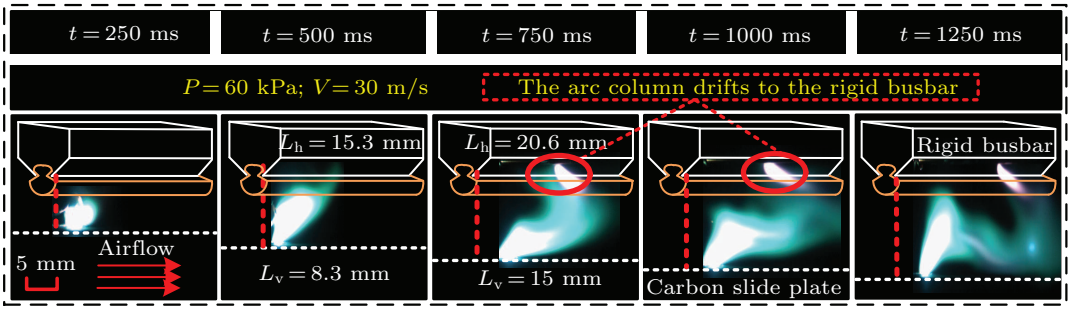


Fig. 3. Development process of pantograph-catenary arc (P = 60 kPa, V = 30 m/s).

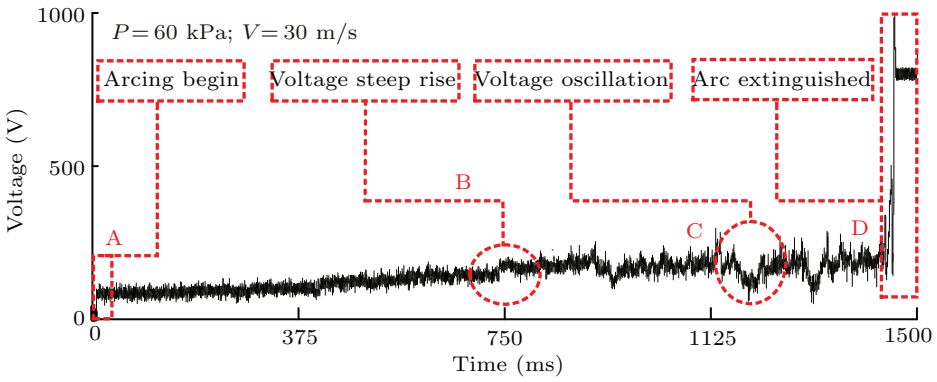


Fig. 4. Voltage waveform (P = 60 kPa, V = 30 m/s).

Figure 4 shows the pantograph-catenary arc voltage waveform when P = 60 kPa and V = 30 m/s. A comprehensive analysis of the voltage waveform shows four stages: a voltage jump-slowly rising-voltage steep rise-frequent oscillation. Before the separation of the carbon and copper electrodes, the electrodes are in contact, and the voltage between the electrodes is about 0 V. With the separation of the carbon electrode and the copper electrode, arcing begins, and the inter-electrode voltage is transformed into the arc voltage, showing a steep rise in the voltage waveform as shown in area A. In stages A to B, the rising rate of the voltage waveform increases significantly, and the voltage amplitude increases from about 150 V to about 210 V. This is because the wind load and thermal buoyancy of the arc increase significantly, and the arc length and the vertical drift height increase, resulting in a rapid increase in arc voltage. In stages B to D, with the further increase of the arc length, the stability of the arc column deteriorates, and the voltage waveform shows a trend of frequent oscillation.

It is worth noting that the voltage surge and oscillation phenomena can be seen in the voltage waveform, as shown in areas B and C. The analysis shows that in area B, the anode arc root jumps from the catenary to the busbar, the arc length increases instantaneously, and the arc voltage rises sharply. The

reason for the oscillating change of the voltage waveform in area C is the root jumping behavior of the anode arc root. During the arc root jumping process, the newly formed arc channel is shorter than the original arc channel, and the arc voltage drops rapidly. After the arc root jump is completed, the new arc channel develops stably, and the arc voltage gradually returns to the original amplitude, showing a dynamic change of oscillation on the voltage waveform.

3. Arc column vertical drift movement influences mechanism

3.1. Characteristics of arc column vertical drift

The characteristic curves of arc vertical drift height-time under different air pressure and airflow are statistically analyzed, as shown in Fig. 5. Figure 5(a) shows the variation of the arc vertical drift height with time when the airflow velocity is 30 m/s and the air pressure is 60 kPa and 80 kPa, respectively. When the arc develops from the start of arcing ($t = 0$ ms) to about 500 ms, the arc column vertical drift shows a trend of uniform development. Between 500 ms and 700 ms, the vertical arcing speed increases significantly. When the arcing time is about 750 ms, the anode root jumps to the rigid busbar, and the height of the arc column is close to the distance between the busbar and the carbon slide. On the contrary, when the air pressure is 80 kPa, the arc column develops to the busbar when the arcing time is about 800 ms.

The air pressure is inversely proportional to the arc vertical drift height. The arc vertical drift higher, and the arc column is easier and faster to develop to the busbar under low air pressure. There are two possible reasons: on the one hand, the diameter of the arc column becomes larger under low air pressure, and the thermal buoyancy of the arc is proportional to the arc radius, so the thermal buoyancy of the arc is greater. On the other hand, the arc length is longer under low air pressure, which also promotes the increase of thermal buoyancy on the arc. Therefore, the arc column drifts higher under low air pressure, and it is easier to drift to the busbar.

Figure 5(b) shows the characteristic curves of arc vertical drift height-time for the airflow velocities of 20 m/s and 30 m/s. When the airflow velocity is 30 m/s, the arc vertical drift is faster than that when the airflow velocity is 20 m/s. The possible reasons for the higher height and speed of the arc vertical drift under the strong airflow velocity are as follows: The influence of airflow velocity on the arc column is greater than the influence on the arc root. Under the condition of strong airflow, the wind load on the arc column is larger, the arc column is rapidly stretched under the action of wind load, and the arc length increases rapidly. The overall thermal buoyancy of the arc column can be regarded as the vertical upward thermal buoyancy of each arc column unit. Therefore, under the condition of strong airflow, the thermal buoyancy of the arc is greater, and the arc column vertical drift is more serious.

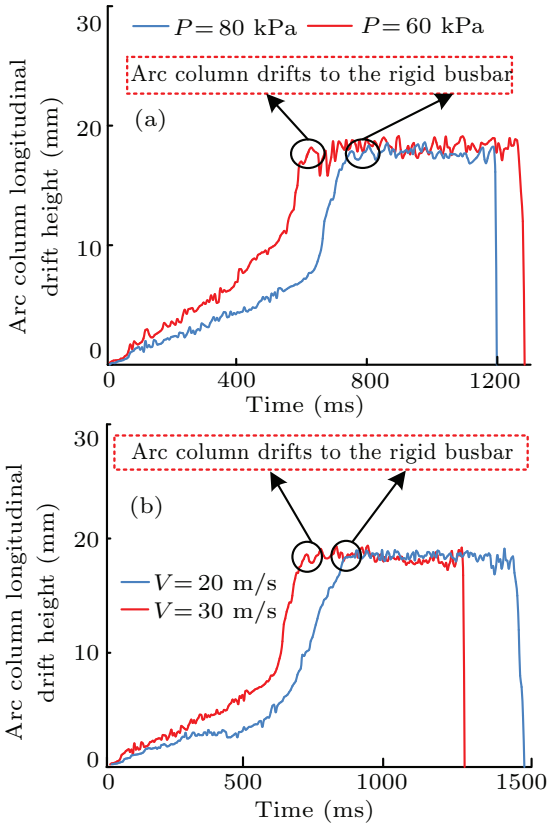


Fig. 5. Variation of arc vertical drift height under different pressure and airflow: (a) different pressure, (b) different airflow.

3.2. The development process and the physical mechanism of arc column drift to the busbar

Given the development characteristics of the arc column drifting on the busbar found in the above analysis, the dynamic process of the arc column drifting to the busbar when the air pressure is 60 kPa and the airflow velocity is 30 m/s was captured by a high-speed camera, as shown in Fig. 6. The arc drifting to the busbar is divided into three processes: arc column heating the busbarthe new arc root forming the original arc root extinguishing. The specific analysis is as follows: when the arc develops to about $t = 700.0$ ms, it can be seen that the arc column vertically drifts to the position of busbar A, and continues to heat the busbar, resulting in an aggravated temperature rise of the busbar. When the arcing time is about 712.5 ms, a new arc root is formed at the B position on the busbar. At this time, the new arc root and the original arc root coexist for a short time at positions A and B. Due to the large resistance of the original arc root, it is not enough to maintain the stable combustion of the arc. Therefore, when the arc develops to about $t = 725.0$ ms, the original arc root is extinguished and finally replaced by the new arc root. At this point, the development process of the arc column floating to the busbar is completed.

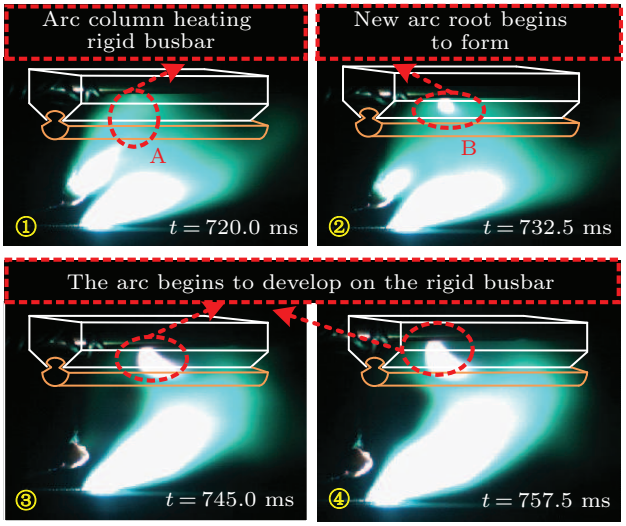


Fig. 6. The dynamic process of the arc column drifting to the busbar.

The physical mechanism of the arc drift easily forming a new arc root on the busbar is analyzed as follows: On the one hand, since the busbar material is mainly aluminum, its work function is smaller than that of the copper electrode, so the arc column floating arc heating the busbar is more likely to cause thermal emission, and it is easy to form a new arc root. On the other hand, at low air pressure, the air breakdown voltage decreases, and the arc drifts to the vicinity of the busbar and is more likely to break down the air, forming a new arc root on the busbar.

3.3. Evolution process and following characteristics of arc root on busbar

To further analyze the development and evolution process of the arc column after the arc column floats to the busbar, the arc development image with the arcing time between about 1000.0 ms and 1062.5 ms is extracted, and the results are shown in Fig. 7. When the arc develops to about 1000.0 ms, the anode root is at position A of the busbar. When the arcing time is about 1012.5 ms, the arc column continues to heat the B position of the busbar due to the arc column's vertical drift. Until $t = 1025.0$ ms, a new anode arc root is formed at the B position of the busbar. At this time, a bright spot can be seen macroscopically. Two anode arc roots exist at positions A and B at the same time, and the coexistence of the double arc roots continues until the arcing time is about 1037.5 ms. Finally, when the arc develops to about $t = 1050.0$ ms, the original arc root is gradually extinguished due to the large resistance of the original arc root, and the anode arc root jumping process is completed.

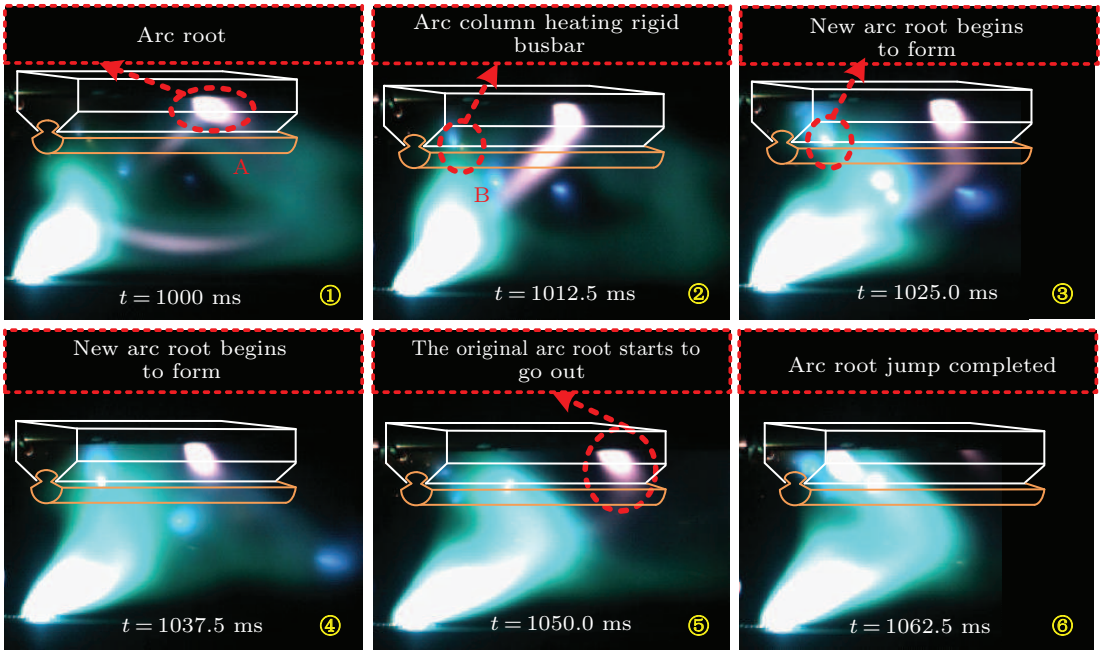


Fig. 7. Arc root jumps on rigid busbar.

4. The multi-field stress coupling model of pantograph-catenary arc under low air pressure and strong airflow

4.1. Multi-stress coupled modeling

In this paper, a multi-stress numerical calculation model of pantograph arc under low air pressure and strong airflow is established based on a chain model, as shown in Fig. 8. The contact wire material and radius used in the model are consistent with the actual wire parameters. The bottom profile radius of the contact line is 6.5 mm, and the length and thickness of the carbon slide are 15 mm and 20 mm, respectively. The initial calculated length of the pantograph arc is set to 4 mm.

During the simulation calculation, the following basic as-

sumptions were used:[31]

(i) It is generally believed that the lateral width of the bright part in the middle of the arc column is the diameter of the arc column.

(ii) The rate of change of the arc diameter is much smaller than the rate of change of the arc length, and the arc diameter of the arc column model is considered to be a constant value.

(iii) In the modeling analysis, a single current element can be regarded as a rigid body, and the diameter of the rigid body of the microcurrent element is considered unchanged.

(iv) During the calculation, when the height of the arc column reaches the busbar, it is determined that a new arc root is formed on the busbar.

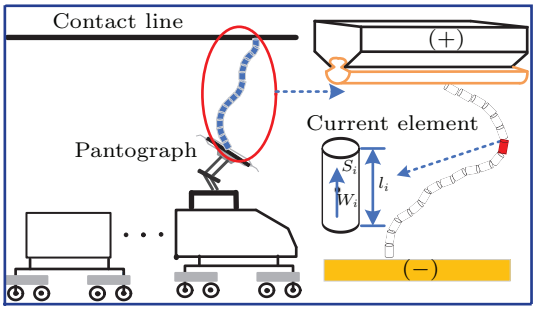


Fig. 8. Schematic diagram of the chain arc model.

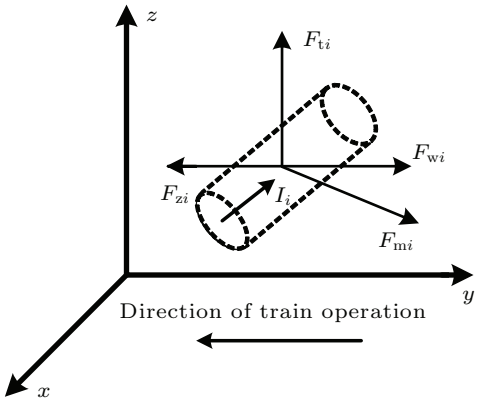


Fig. 9. Schematic diagram of the comprehensive force of the current element.

When calculating the motion state of the arc based on the chain arc model, it is necessary to define the position and direction of each micro-current element of the arc column at the initial moment of calculation. The position of each current element is determined by its center of gravity, and its axial vector and length are determined by two adjacent current elements. For example, the position of the current element W_i is determined by two adjacent current elements W_{i1} and W_{i+1}, where W_i represents the center of gravity coordinate of the arc element, l_i represents the length of the i-th current element, and $\boldsymbol{S}_i$ represents the vector of the arc element. Then, l_i and $\boldsymbol{S}_i$ can be expressed as follows:

$$l_i = \frac{1}{2}\overrightarrow{W_{i-1}W_{i+1}}, \tag{3}$$

$$\boldsymbol{S}_i = \frac{1}{2}\overrightarrow{W_{i+1}-W_{i-1}}. \tag{4}$$

The comprehensive force of a single current element of the chain arc is shown in Fig. 9. Each arc current element is subjected to the combined action of the electromagnetic force $\boldsymbol{F}_{mi}$, wind load $\boldsymbol{F}_{wi}$, thermal buoyancy $\boldsymbol{F}_{ti}$, and air resistance $\boldsymbol{F}_{zi}$ in the whole process of motion development. Based on the chain model, by analyzing the force of each current element, the multi-field stress variation law of the arc as a whole during the moving process can be calculated.

(i) Electromagnetic force model

The electromagnetic field in the space where the pantograph-catenary arc is located comes from the superposition of the magnetic field generated by the current of the catenary wire and the magnetic field generated by the pantograph arc itself. The magnetic induction intensity at the current element i can be expressed as

$$\boldsymbol{B}_i = \boldsymbol{B}_{1i} + \boldsymbol{B}_{2i}. \tag{5}$$

In the formula, $\boldsymbol{B}_i$ is the total magnetic field intensity of the current element; $\boldsymbol{B}_{1i}$ is the magnetic field intensity generated by the catenary wire current; $\boldsymbol{B}_{2i}$ is the electric field intensity generated by the arc itself, then the magnetic induction intensity $\boldsymbol{B}_i$ at the current element i is calculated by the Biot–Savart law.[32] The calculation method can be expressed as follows:

$$\boldsymbol{B}_i = \sum_1^n \boldsymbol{B}_j \times \boldsymbol{D}_{mj}, \tag{6}$$

$$\mathrm{d}\boldsymbol{B} = \frac{\mu_0}{4\pi}\cdot\frac{I\mathrm{d}\boldsymbol{l}\times\boldsymbol{r}}{r^3}, \tag{7}$$

$$B_j = \int_{l_1}^{l_2}\mathrm{d}B = \int_{l_1}^{l_2}\frac{\mu_0}{4\pi}\cdot\frac{I\mathrm{d}I\times r}{r^3} = \frac{\mu_0 I}{4\pi r_0}(\cos\theta_1 - \cos\theta_2)\boldsymbol{e}_B. \tag{8}$$

In the formula, B_j is the scalar value of the magnetic field generated by the current element j at the current element i, and l_1 and l_2 are the start and end points of a single current element i; μ_0 is the vacuum permeability, r is the distance between the position to be determined and the arc current micro-element, r_0 is the vertical distance; the direction of $\boldsymbol{r}$ is the arc micro-element pointing to the point to be determined. θ_1 is the angle between the starting position of the arc micro-element and the point to be calculated, θ_2 is the angle between the end position of the arc micro-element and the point to be calculated, and $\boldsymbol{e}_B$ is the unit vector. The magnetic induction intensity $\boldsymbol{B}_{ai}$ generated by each discretized current element at i is superimposed to obtain $\boldsymbol{B}_{1i}$ and $\boldsymbol{B}_{2i}$, and $\boldsymbol{D}_{mj}$ is the unit vector of the magnetic field. The electromagnetic force can be decomposed into three spatial coordinate axes according to this vector. The self-electromagnetic force $\boldsymbol{F}_{mi}$ on the current element i can be expressed as

$$\boldsymbol{F}_{mi} = \boldsymbol{B}_i \times \boldsymbol{I}_i l_i, \tag{9}$$

where $\boldsymbol{I}_i$ is the current vector flowing through current element i, and l_i is the length of current element i.

(ii) Thermal buoyancy model

The pantograph arc is a thermal plasma, the temperature in the central area of the arc column can be as high as 10000–12000 K, the temperature rise of the air around the arc is equal to the temperature of the arc, and the air density around the arc drops sharply, and the pantograph arc is subjected to vertical upward thermal buoyancy. The buoyancy equation calculates the magnitude of the thermal buoyancy $\boldsymbol{F}_{\mathrm{t}i}$ on the current element i,

$$\boldsymbol{F}_{\mathrm{t}i} = (\rho_0 - \rho) \cdot g\pi r_i^2 l_i \boldsymbol{D}_{\mathrm{t}i}. \tag{10}$$

In the formula, g is the acceleration of gravity, $g = 9.8$ m/s^2; ρ_0 is the air density under standard atmospheric pressure; ρ is the air density around the arc column; r_i is the radius of the current element arc column; l_i is the length of the current element; the thermal buoyancy direction $\boldsymbol{D}_{\mathrm{t}i}$ is vertically upward. r_i changes with the decrease of air pressure. Therefore, this paper corrects the thermal buoyancy calculation method under different air pressures, in which the arc radius is corrected according to

$$r_i = \left(\frac{P}{P_0}\right)^{-0.465} \sqrt{\frac{I}{1.45\pi}}. \tag{11}$$

The air density is thin at low air pressure, and the relationship between relative air density and air pressure at low air pressure can be expressed as Eq. (12), where t is the air temperature around the arc column of the pantograph arc under pressure P,

$$\sigma = \frac{\rho_{\mathrm{P}}}{\rho_0} = \frac{P}{P_0} \times \frac{293}{273+t}. \tag{12}$$

Therefore, the thermal buoyancy can be expressed as

$$\boldsymbol{F}_{\mathrm{t}i} = \left(\rho_0 - \frac{P}{P_0} \times \frac{293}{273+t} \times \rho_0\right) \cdot g\pi r_{\mathrm{a}i}^2 l_{\mathrm{a}i}. \tag{13}$$

(iii) Wind load

During the actual operation of the high-speed train, it has always been in a strong airflow environment caused by the train wind. The pantograph-catenary arc generated by the separation of the contact line and the pantograph slide plate during the train operation is affected by the wind load opposite to the train's running direction. In the simulation calculation, it is considered that the magnitude and direction of the airflow velocity received by the arc column within a calculation time step remain unchanged. The wind load $\boldsymbol{F}_{\mathrm{w}i}$ on the current element i can be expressed as

$$\boldsymbol{F}_{\mathrm{w}i} = \frac{1}{2}\beta_z \mu_{\mathrm{s}} \mu_z r_i l_i \rho v_{\mathrm{w}}^2 \cdot \boldsymbol{D}_{\mathrm{w}i}, \tag{14}$$

where β_z is the wind vibration coefficient, μ_{s} is the body shape coefficient, μ_z is the wind pressure height variation coefficient, v_{w} represents the airflow velocity scalar, and $\boldsymbol{D}_{\mathrm{w}i}$ represents the airflow velocity unit vector, according to which the wind load can be decomposed into three spatial coordinate axes.

(iv) Air resistance

The pantograph arc is affected by the air resistance opposite to the movement direction in the movement space. The air resistance $\boldsymbol{F}_{\mathrm{a}i}$ on the current element i can be expressed as

$$\boldsymbol{F}_{\mathrm{a}i} = C_r r_i l_i \rho v_i^2 \cdot \boldsymbol{D}_{\mathrm{v}i}, \tag{15}$$

where C_r is the air resistance coefficient, v_i is the scalar of the velocity of the current element i, and $\boldsymbol{D}_{\mathrm{v}i}$ is the unit vector of the velocity of the current element i. Air resistance can be decomposed into three spatial axes according to this vector.

$$\boldsymbol{F}_{\mathrm{b}i} + \boldsymbol{F}_{\mathrm{m}i} + \boldsymbol{F}_{\mathrm{t}i} + \boldsymbol{F}_{\mathrm{w}i} + \boldsymbol{F}_{\mathrm{a}i} = m_i \cdot \boldsymbol{a}_i, \tag{16}$$

where m_i and a_i are the mass and the acceleration vector of current element i, respectively. Because the mass of a single current element is extremely small, in addition, as long as the simulation time step is small enough, the acceleration is considered to be 0 in the calculation time step. Therefore, we can obtain

$$v_i^2 = \frac{\sqrt{(\boldsymbol{F}_{\mathrm{m}i} + \boldsymbol{F}_{\mathrm{b}i} + \boldsymbol{F}_{\mathrm{t}i} + \boldsymbol{F}_{\mathrm{w}i})^2}}{C_r r_i l_i \rho}. \tag{17}$$

From this, the velocity scalar of the current element i can be achieved. The motion velocity unit vector $\boldsymbol{D}_{\mathrm{v}i}$ of the current element i is determined by $\boldsymbol{D}_{\mathrm{m}j}$, $\boldsymbol{D}_{\mathrm{w}i}$, and $\boldsymbol{D}_{\mathrm{t}i}$.

4.2. Model validation

To verify the accuracy of the multi-stress coupling model of the pantograph-catenary arc with low air pressure and strong airflow, the arc motion image obtained by the numerical model simulation calculation and the experimental arc motion image were compared and analyzed, and the comparison results are shown in Fig. 10. It can be found that the simulated images of the pantograph-catenary arc are very consistent with the experimental arc images. This also shows that the multi-stress coupling model of the pantograph-catenary arc established in this paper is real and effective. Based on this model, the internal multi-stress variation law and action mechanism of arc motion drifting arc can be explored.

5. Multistress mechanism of arc drift

5.1. Multi-stress variation law of arc under low air pressure and strong airflow

The multistress variation laws of the electromagnetic force, wind load, thermal buoyancy, etc. are calculated when the air pressure is 60 kPa and the airflow velocity is 30 m/s, as shown in Fig. 11. As can be seen from the figure, electromagnetic force, wind load, and thermal buoyancy with the arc burning time show a phase distribution characteristic.

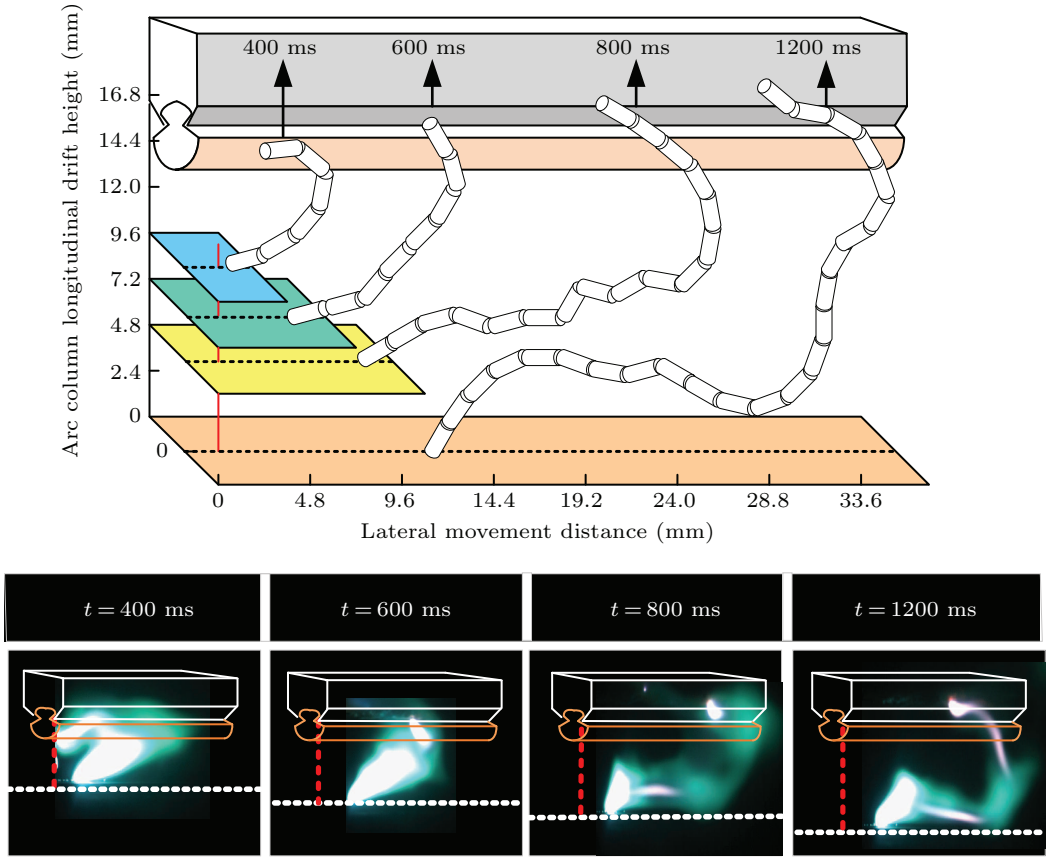


Fig. 10. Results in comparison of simulation (a) and experiment (b).

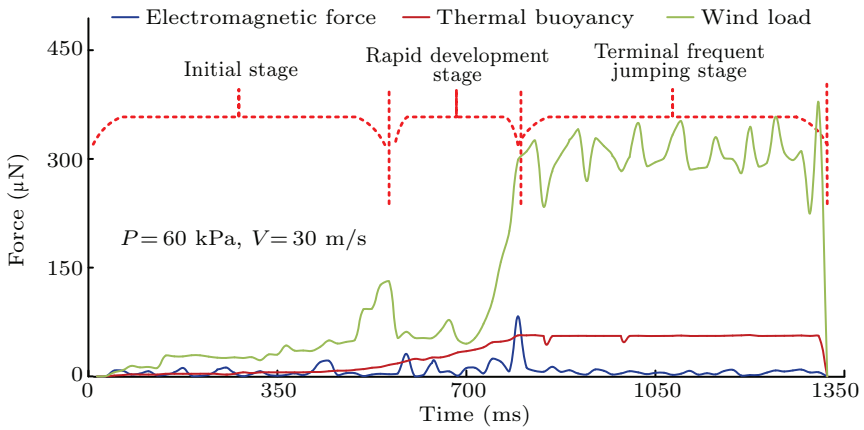


Fig. 11. Multi-stress variation law of arc with time.

At the initial stage of arcing, the wind load, thermal buoyancy, and electromagnetic force on the arc are the same, and the wind load is slightly greater than the electromagnetic force and thermal buoyancy. Because the tensile effect of wind load on the arc column is not obvious in this stage, the arc develops to the right relative to the arc starting position as a whole, and the motion form presents a random motion state of self-spiral. It can be seen from the rapid development stage in the figure that the wind load and thermal buoyancy increase rapidly, but the acceleration of wind load growth is greater than that of thermal buoyancy growth. Because the arc length further increases with the continuous separation between the copper electrode and the carbon slide plate of the pantograph catenary arc, the wind load on the arc is proportional to the arc length, and the wind load on the arc increases rapidly. In addition, the thermal buoyancy increases with the increase of arc length, and the arc column begins to appear an obvious arc floating phenomenon, and it floats to the busbar for development at about 750 ms, which happens to be in the rapid development stage of wind load and thermal buoyancy calculated by the multi stress model. This also verifies the validity of the calculation model and the accuracy of the multi-stress calculation results.

It is worth noting that in the frequent oscillation stage,

the electromagnetic force is significantly lower than that in the rapid development stage. In this stage, the arc length is close to the maximum arc length that can be maintained by the voltage and current, the arc stability becomes worse, the identity of each current element in the moving space becomes worse, and the electromagnetic forces received by each current element partially offset each other, so the electromagnetic force becomes smaller on the whole.

5.2. Multistress variation of arc under different air pressure and its influence mechanism

Figure 12 shows the variation law of electromagnetic force for the air pressures of 60 kPa and 80 kPa. It is found that there is little difference between the two groups of electromagnetic force in terms of amplitude or distribution trend in time scale under different air pressure, that is, it fluctuates in a small amplitude range at the beginning and end of arcing. In the middle stage of arcing process, the electromagnetic force reaches the maximum value, and the maximum amplitude is about 24 μN. The specific analysis is stated in the following.

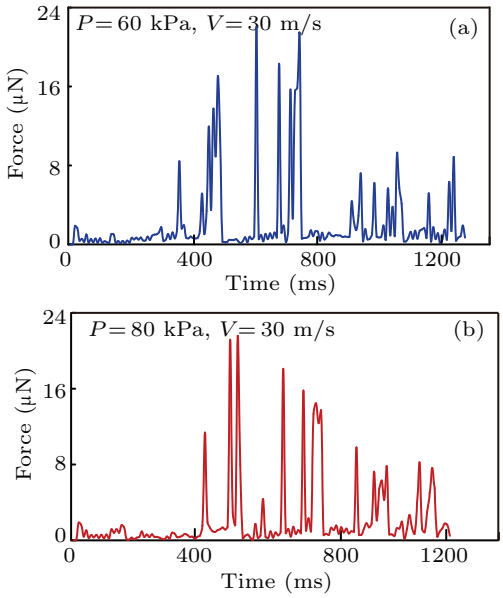


Fig. 12. Variation law of electromagnetic force at different air pressures: (a) $P = 60$ kPa, (b) $P = 80$ kPa.

In the initial stage of arcing, the arc column is short. Even though the identity of each current element in the moving space is high, the electromagnetic force on the arc as a whole still fluctuates in a small amplitude range. In the rapid development stage of arcing, the arc length increases rapidly, and the movement direction of each current element of the arc is highly identical. Therefore, the overall electromagnetic force on the arc is the largest in the whole arcing process. In the end stage of arcing, although the arc length is further increased, the arc stability is the worst, the identity of the movement direction between the current elements of the arc is the lowest, and the arc electromagnetic force is significantly reduced.

The air pressure class has little effect on the electromagnetic force of the arc. The possible reason is that there is a competitive relationship between arc current and arc length under different pressure. At lower pressure, the vertical arc height and arc length are higher, which promotes the increase of electromagnetic force amplitude at low air pressure. At the same time, the arc current is smaller at lower pressure, which weakens the increase of electromagnetic force amplitude at lower pressure. Therefore, under the combined action of the arc height and arc length, the electromagnetic force amplitude and variation trend of the arc are the same under different pressure levels.

The variation law of arc thermal buoyancy under different air pressures is calculated, as shown in Fig. 13(a). The thermal buoyancy at 60 kPa is greater than that at 80 kPa in the whole arcing stage, and the growth rate of thermal buoyancy is higher at the low air pressure and reaches the maximum value at about 800 ms of arcing time, the maximum value is about 56 μN. When the air pressure is 80 kPa, the time lag to reach the maximum value is about 200 ms, and the maximum value is about 44 μN.

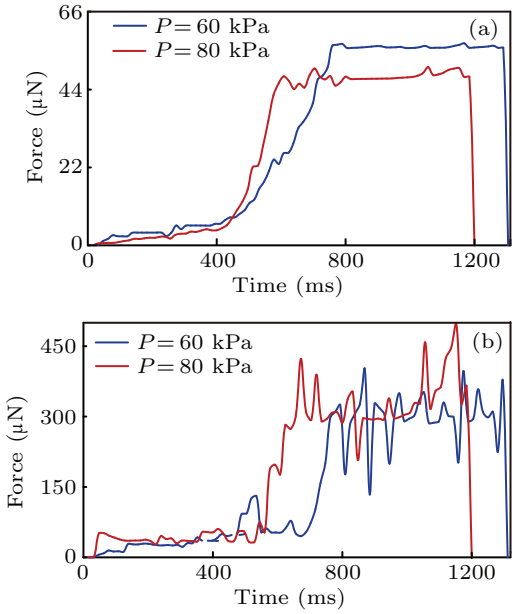


Fig. 13. Variation law of thermal buoyancy and wind load at different air pressures: (a) thermal buoyancy, (b) wind load.

The possible reasons for the high thermal buoyancy of the arc under low air pressure are as follows: The arc thermal buoyancy is mainly determined by the arc radius and arc length. When the air velocity is constant, the arc length at different pressures has little difference, but the arc radius is larger at the low air pressure, so the thermal buoyancy is greater.

Figure 13(b) shows the variation law of wind load under different air pressures. In the initial stage of the arc, there is no obvious horizontal stretching and vertical drift of the arc at this time. The arc length has little difference under different

pressure levels. Therefore, the wind load at 60 kPa is equivalent to that at 80 kPa. In the rapid development stage of arcing, because the arc column diameter is large and the arc develops slowly under low air pressure, the arc wind load is small when the pressure is 60 kPa, and its rapid growth stage lags about 150 ms. At the end of the arc, the arc develops to the busbar, and the arc length is similar under different air pressure levels. Therefore, there is little difference in the amplitude of wind load on the arc at this stage.

5.3. Multi-stress coupled modeling

The physical mechanism of the pantograph-catenary arc easily drifts to the rigid busbar in low air pressure and a strong airflow environment is further revealed, as shown in Fig. 14. The physical mechanism of arc drifting arc is analyzed as follows:

(i) In the initial stage of arcing (0–400 ms), there is no obvious horizontal stretching and vertical drift of the arc at this time. The arc voltage waveform is shown in inset A of Fig. 14, the arc voltage increases slowly, and the arc voltage is maintained at about 90 V. In addition, the electromagnetic force, wind load, and thermal buoyancy of the arc are relatively small, the arc length is approximately the distance between the carbon–copper electrodes, and the growth rate of the floating arc height is approximately equal to the cathode descending speed.

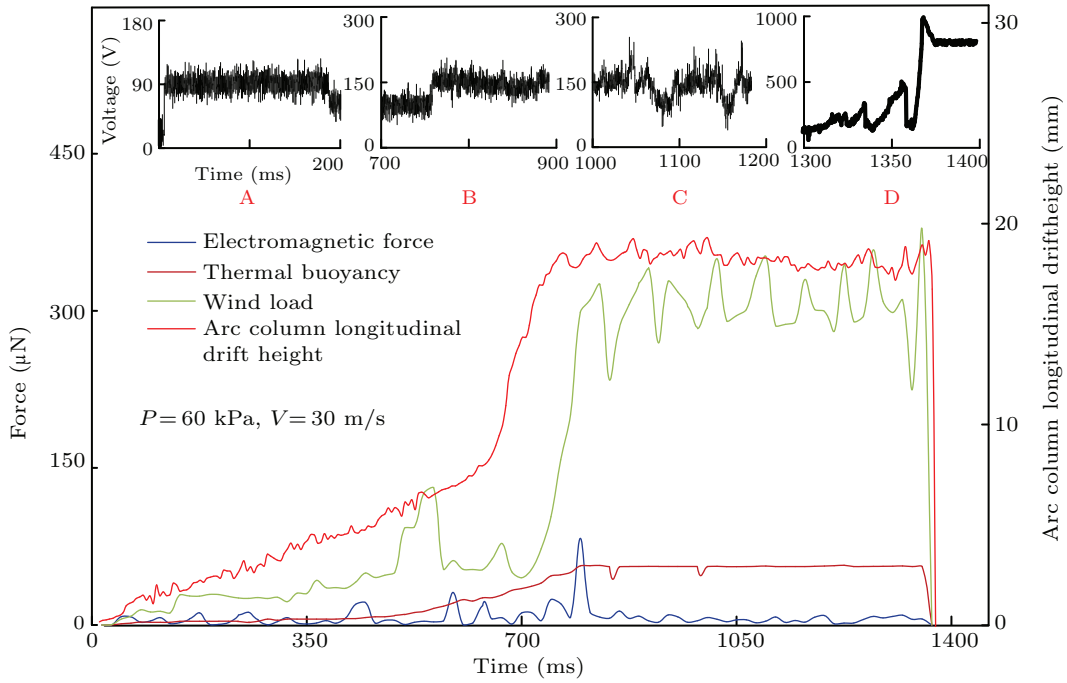


Fig. 14. Physical mechanism of pantograph-catenary arc drift to the rigid busbar.

(ii) In the rapid development stage (400 ms–800 ms), the wind load and thermal buoyancy increase rapidly, but the acceleration of wind load growth is greater than that of thermal buoyancy. In addition, the thermal buoyancy of the arc column increases with the increase of the arc length, the arc column begins to vertically drift significantly. Combining the arc images and voltage waveforms, it can be found that it drifts to the busbar at about 750 ms and develops, which is exactly at the stage of rapid development of the wind load and thermal buoyancy calculated by the multi-stress model. On the other hand, the validity of the calculation model and the accuracy of the multi-stress calculation results are verified.

(iii) The wind load at this stage oscillates with the increase and decrease of the arc length. The overall change of thermal buoyancy is stable, and there is no obvious increasing trend. Compared with the rapid development stage, the electromagnetic force is significantly reduced. This is not because the arc current has changed significantly, but mainly because the arc column frequently swings laterally from side to side at this stage, and the uniformity of the motion direction of each current element becomes worse. The electromagnetic force received by each current element cancels each other, so the electromagnetic force as a whole becomes smaller.

6. Conclusion and perspectives

(i) The characteristics of pantograph-catenary arc drifting under low air pressure and strong airflow have been explored, the vertical drift height-time curve under different air pressures and airflow velocities is established, and the stage distribution characteristics of pantograph-catenary arc vertical drifting are analyzed. It is found that the air pressure is inversely proportional to the arc vertical drift height, and the airflow velocity is proportional to the arc vertical drift height. The fundamen-

tal reason why the arc is more likely to develop to the busbar under low air pressure and strong airflow is theoretically analyzed.

(ii) The physical process of the arc column drift to the busbar is summarized and analyzed. The arc floating to the busbar goes through three stages under low air pressure: arc column heating busbar-new arc root formation-original arc root extinction. It is found that the promotion of heat emission and the reduction of air breakdown voltage under low air pressure are the main reasons why new arc roots are easily formed on the busbar under low air pressure.

(iii) The arc development process and the jumping characteristics of the arc root on the busbar are explored. The arc movement on the busbar is mainly completed in the form of arc root jumping. It is revealed that the arc root has a polarity effect, which leads to the rapid development of the anode arc root on the busbar.

(iv) Considering the coupling effect of multi-physics comprehensively, a multi-stress coupling model of pantograph-catenary arc in low air pressure and strong airflow is established, and the accuracy of the simulation model is verified by comparison with experiments. The multi-stress variation law during the arc motion is quantitatively calculated, and the influence mechanism of air pressure on the arc comprehensive stress is clarified. The physical mechanism of pantograph-catenary arc drift in the low air pressure and strong airflow environment is comprehensively analyzed from the aspects of the voltage waveform, vertical drift height-time curve, and multi-field stress changes.

Acknowledgements

Project supported by the National Natural Science Foundation of China (Grant Nos. 51707166, 51922090, U1966602, and U19A20105), and the Sichuan Science and Technology General Project (Grant Nos. 2019YJ0213 and 2019JDJQ0019).

References

[1] Huang J, Yang L, Zhang H C, Chen L and Wu X Y 2019 *Chin. Phys. B* **28** 055202
[2] Lin Q F, Zhao Y J, Duan W X, Ni G H, Jin X Y, Sui S Y, Xie H B and Meng Y D 2020 *Chin. Phys. B* **29** 125201
[3] Luo L L, Ye X Q, Zhang G H, Kou H Q, Xiong R J, Sang G, Yu R H and Zhao D L 2020 *Chin. Phys. B* **29** 088801
[4] Zhang G P, Wang X Q, Lü G H, Zhou L, Huang J, Chen W and Yang S Z 2013 *Chin. Phys. B* **22** 035204
[5] Zhang Z L, Wang C, Sun Q and Xia W D 2019 *Chin. Phys. B.* **28** 095201
[6] Wei W F, Zhang T T, Gao G Q and Wu G N 2018 *High Voltage Eng.* **44** 1589 (in Chinese)
[7] Gao G Q, Hao J, Wei W F, Hu H X, Zhu G Y and Wu G N 2016 *IEEE Trans. Plasma Sci.* **44** 2715
[8] Wu G N, Zhou Y, Lei D, Wei W F, Wu J and Gao G Q 2016 *High Voltage Eng.* **42** 3495 (in Chinese)
[9] Hejripour F, Valentine D T and Aidun D K 2018 *Int. J. Heat Mass Transfer* **125** 471
[10] Xie W H, Wu G N, Yang Z F, She P P, Wang H, Zuo H Z and Tu C J 2021 *High Volt.* **6** 674
[11] Xu Z L, Gao G Q, Wei W F, Yang Z F, Xie W H, Dong K L, Ma Y G and Wu G N 2022 *High Volt.* **7** 369
[12] Yin J N, Wang Q and Li X W 2018 *IEEE Trans. Plasma Sci.* **46** 2788
[13] Rong M Z, Zhong L L, Wang X H and Gao Q Q 2016 *Trans. China Electrotech. Soc.* **31** 54
[14] Mao H Y, Chang G, Zhu X G and Wang Y 2007 *IEEE Trans. Dielectr. Electr. Insul.* **14** 179
[15] Lin X, Wang N and Xu J Y 2013 *Plasma Sci. Technol.* **15** 644
[16] Chen Y, Yang F, Sun H, Wu Y, Niu C P and Rong M Z 2017 *Plasma Sci. Technol.* **19** 24
[17] Chen W J, Yan X L, He Z M and Li Z B 2010 *High Voltage Eng.* **36** 1 (in Chinese)
[18] Sun Q Q, Li Q M, Chen Q and Cong H S 2012 *High Voltage Eng.* **38** 350 (in Chinese)
[19] Gao G Q, Hao J, Wei W F, Hu H X, Zhu G Y and Wu G N 2016 *IEEE Trans. Plasma Sci.* **44** 2715
[20] Hao J and Gao G Q 2018 *J. China Railway Soc.* **40** 65
[21] Hao J, Gao G Q, Xu P, Wei W F and Wu G N 2018 *High Voltage Eng.* **44** 1668 (in Chinese)
[22] Wei W F, Wu J, Gao G Q, Gu Z, Liu X R, Zhu G Y and Wu G N 2016 *IEEE Trans. Plasma Sci.* **44** 2438
[23] Gao G Q, Xu P, Wei W F, Yang Z F, Hu Y and Wu G N 2019 *High Voltage Eng.* **45** 3916 (in Chinese)
[24] Yang Z F, Xu P, Wei W F and Gao G Q 2020 *IEEE Trans. Plasma Sci.* **48** 2822
[25] Zhu G Y, Gao G Q, Wu G N and Gu Z 2015 *Proceedings of the Institution of Mechanical Engineers, Part F: Journal of Rail & Rapid Transit* **230** 1687
[26] Xu P, Yang Z F, Wei W F, Gao G Q and Wu G N 2018 *AIP. Adv.* **8** 115008
[27] Zhou Y H, Yang Z F, Lu C, Mu T Y, Wei W F, Gao G Q and Wu G N 2021 *Proc. CSEE* **41** 5412 (in Chinese)
[28] Cao J W, Huang H J and Pan W X 2014 *Chin. Phys. Lett.* **31** 115202
[29] Benilov M S, Hartmann W, Kaufmann H T C and Benilova L G 2018 *2018 28th International Symposium on Discharges and Electrical Insulation in Vacuum (ISDEIV)*, September 23–28, 2018, Greifswald, Germany, pp. 353–356
[30] Zhang Z J, Jiang X L, Sun C X, Hu J L and Yuan J H 2009 *Proc. CSEE* **29** 104 (in Chinese)
[31] Cong H X, Li Q M, Xing J Y and Siew W H 2015 *IEEE Trans. Plasma Sci.* **43** 2046
[32] Gu S Q, He J L, Chen W J and Xu G Z 2006 *Proc. CSEE* **26** 140 (in Chinese)